Explicit expression of mesophyll conductance in the traditional leaf photosynthesis–transpiration coupled model and its physiological significances

Hong Luo[1], Marc Carriquí[2], Miquel Nadal[2], Tuo Han[3], Christiane Werner[4], Jian-feng Huang[5], Jiao-lin Zhang[5], Zhi-guo Yu[6], Feng-min Li[1], Xiang-wen Fang[1], Wei Xue[1*]

[1]College of Earth and Environmental Sciences, School of Life Sciences, State Key Laboratory of Grassland Agroecosystems, Lanzhou University, Lanzhou730000, China

[2]Research Group in Plant Biology under Mediterranean Conditions, Agro-Environmental and Water Economics Institute, Universitat de les IllesBalears, Palma, IllesBalears 07122, Spain

[3]The Northwest Institute of Eco-Environment and Resources, Chinese Academy of Sciences, Lanzhou730000, China

[4]Department of Ecosystem Physiology, University of Freiburg, Freiburg 79110, Germany

[5]Key Laboratory of Tropical Forest Ecology, Xishuangbanna Tropical Botanical Garden, Chinese Academy of Sciences, Mengla 666303, China

[6]Nanjing University of Information Science and Technology, School of Hydrology and Water Resources, Nanjing 210044, China

*Author for correspondence: Wei Xue, Tel: 0931-8912560; Email: xuewei@lzu.edu.cn

Total word count (excluding summary, references and legends):	6480	No. of figures:	4 (all of Fig in color)
Summary:	180	No. of Tables:	2
Introduction:	841	No. of Supporting Information	16 (Figs. S1–S10; Tables S1–S6)

		files:	
Materials and Methods:	1936		
Results:	1669		
Discussion:	2034		

1 **Explicit expression of mesophyll conductance in the traditional leaf**

2 **photosynthesis–transpiration coupled model and its physiological significances**

3

4

5 **Summary**

6 ● Almost all terrestrial biosphere models (TBMs) still assume infinite mesophyll

7 conductance (g_m) to estimate photosynthesis and transpiration. This assumption has

8 caused low accuracy of TBMs to predict leaf gas exchange under certain conditions.

9 ● Here, we developed a photosynthesis–transpiration coupled model that explicitly

10 considers g_m and designed an optimized parameterization solution through

11 evaluating four different g_m estimation methods in 19 C_3 species at 31 experimental

12 treatments.

13 ● Temperature responses of the maximum carboxylation rate (V_{cmax}) and the electron

14 transport rate (J_{max}) estimated using the Bayesian retrieval algorithm and the

15 Sharkey online calculator and g_m temperature response estimated using the

16 chlorophyll fluorescence–gas exchange method and anatomy method predicted leaf

17 gas exchange better. The g_m temperature response exhibited activation energy (ΔH_a)

18 of 63.13 ± 36.89 kJ mol^{-1} and entropy (ΔS) of 654.49 ± 11.36 J K^{-1} mol^{-1}. The g_m

19 optimal temperature ($T_{opt\_g_m}$) explained 58% of variations in photosynthesis

20 optimal temperature (T_{optA}). The g_m explicit expression has equally important

21 effects on photosynthesis and transpiration estimations.

22 ● Results advanced understandings of better representation of plant photosynthesis

23 and transpiration in TBMs.

24

25 **Keywords:** mesophyll conductance, photosynthesis, terrestrial biosphere models,

26 temperature response, transpiration

27

28

29 **Introduction**

The leaf photosynthesis–transpiration coupled model is the basis of vegetation photosynthesis and transpiration estimations performed using terrestrial biosphere models (TBMs) (Dai *et al*., 2003; Rogers *et al*., 2017). The model is based on the biochemical-based photosynthesis theory developed by Farquhar *et al*. (1980), which considers the leaf stomatal aperture as the primary gauge of CO_2 influx and water vapor efflux and assumes an infinite conductance of CO_2 diffusion from sub-stomatal cavities to the chloroplast stroma (i.e. mesophyll conductance, g_m). In such cases, there is no CO_2 concentration drawdown between the intercellular airspace and the chloroplast stroma. However, now it is widely accepted not only that there is a significant CO_2 diffusion drawdown from the intercellular airspace to the chloroplast stroma, but that the resistance that causes this drawdown can be similar or greater than stomatal resistance in land plants (Flexas *et al*., 2012; Evans and von Caemmerer, 2013; von Caemmerer and Evans, 2015; Gago *et al*., 2019). Currently, almost all TBMs do not explicitly consider g_m (Rogers *et al*., 2017; Knauer *et al*., 2019; 2020; Iqbal *et al*., 2021), primarily because of (1) huge disputes in response characteristics of g_m to ambient environment, particularly the temperature response (von Caemmerer and Evans, 2015; Bahar *et al*., 2018; Shrestha *et al*., 2019; Li *et al*., 2020; Evans, 2021), and (2) lack of a g_m finite photosynthesis–transpiration coupled model that can be applied to as many C_3 species as possible (Niinemets *et al*., 2009; Xue *et al*., 2017; Knauer *et al*., 2020).

Mesophyll conductance cannot be directly measured mainly because it is not possible to determine the CO_2 concentration within the chloroplast stroma. Thus, modeling methods are required to estimate g_m, which could be grouped into four classes according to the algorithm principle and field measurement tools: the chlorophyll fluorescence–gas exchange method (i.e. g_{m_F}) (Harley *et al*., 1992); the anatomy method (i.e. g_{m_A}) (Tosens *et al*., 2012; Tomas *et al*., 2013); the ^{13}C isotope discrimination method (Evans *et al*., 1986; Barbour *et al*., 2007; Pons *et al*., 2009; Evans and von Caemmerer, 2013; Flexas *et al*., 2013); and the curve-fitting parameter retrieval methods (Sharkey *et al*., 2007; von Caemmerer *et al*., 2009; Gu *et al*., 2010; Zhu *et al*., 2011; von Caemmerer, 2013, Han *et al*., 2020). These methods have their

own advantages and weakness in terms of model parameter assumptions, resulting in large discrepancies in the estimated temperature response of g_m (Pons *et al.*, 2009; Evans, 2021). Therefore, we decided to select the best g_m estimation method in terms of accuracy in predicting leaf gas exchange at any temperature, namely a good criterion to select at each temperature which g_m estimation method works best is the one that could predict leaf gas exchange more accurately.

Effects of the g_m finite expression on photosynthesis have been widely demonstrated, whereas few attentions are paid on transpiration. Considering the indirect effects of g_m on transpiration and the direct effect on photosynthesis through its control on chloroplast CO_2 concentration, Knauer *et al.* (2020) determined that g_m has a greater effect on photosynthesis but no significant effects on transpiration in most species and hence proposed the 'the asymmetric effects on photosynthesis and transpiration estimations' hypothesis. Kumarathunge *et al.* (2019) found that variations in photosynthesis optimal temperature (T_{optA}) can be primarily explained by changes in the ratio of the apparent maximum electron transport rate and the apparent maximum carboxylation rate at 25°C ($J_{a,25}/V_{a,25}$, JVr), thus proposing 'the JVr biochemical limitations' hypothesis. $J_{a,25}$ and $V_{a,25}$ estimations in their study were derived from the A_n/C_i curve without explicitly considering g_m. Previous results indicated significant changes in T_{optA} under different intercellular CO_2 concentrations (C_i) in C_3 species (Farquhar *et al.*, 1980; Rogers *et al.*, 2017), suggesting that the CO_2 substrate levels significantly affect T_{optA}. The CO_2 substrate levels inside the chloroplasts in turn are strongly controlled by g_m. We speculated that the plausibility of the T_{optA}–JVr relationship reported by Kumarathunge *et al.* (2019) is questionable in reality. The observed variations in T_{optA} among plant species may not be solely explained by biochemical limitations.

As a first step towards the better representation of plant photosynthesis and transpiration in most TBMs, we attempted to develop a g_m finite model that could be directly implemented in most TBMs, in addition to design an optimized parameter configuration solution that is physiologically meaningful and can be applied to as many

3

88   C_3 species as possible. The optimized parameterization solution was designed by

89   comparing multiple different parameter estimation methods used for g_m, V_{cmax}, and J_{max}

90   estimations. The response features of g_m, V_{cmax}, and J_{max} to temperature were therefore

91   determined. Validation of the predictability of the g_m finite model compared to a

92   traditional photosynthesis model assuming infinite g_m (abbreviated as the g_m infinite

93   model) was performed in 19 C_3 species under 31 experimental conditions. The effects

94   of the g_m finite expression on leaf photosynthesis and transpiration estimations were

95   quantified to evaluate the 'the JVr biochemical limitations' hypothesis proposed by

96   Kumarathunge *et al*. (2019) and 'the asymmetric effects on photosynthesis and

97   transpiration estimations' hypothesis proposed by Knauer *et al*. (2020).

98

99   **Materials and methods**

100   **Model description**

101   In line with the photosynthesis–transpiration coupled model adopted by most

102   TBMs, the Farquhar, von Caemmerer & Berry (1980) (FvCB) photosynthesis model

103   and a stomatal conductance sub-model (Ball *et al*., 1987; Leuning, 1995) were coupled

104   to quantify leaf carbon uptake and water loss through transpiration. A_n is limited either

105   by the Rubisco carboxylation rate at a low CO_2 concentration (W_c) or the RuBP

106   regeneration rate at a relatively high CO_2 concentration because of low electron

107   transport rates (W_j) or deficit inorganic phosphate for photophosphorylation (W_p). A_n

108   can be expressed as follows:

109   $$A_n = \left(1 - \frac{\Gamma^*}{C}\right) \min\{W_c, W_j, W_p\} - R_d \qquad \text{(Eqn 1)}$$

110   $$W_c = \frac{V_{cmax}C}{C + K_c(1 + O/K_o)} \qquad \text{(Eqn 2)}$$

111   $$W_j = \frac{JC}{4(C + 2\Gamma^*)} \qquad \text{(Eqn 3)}$$

112   $$W_p = 3TPU \qquad \text{(Eqn 4)}$$

113   where V_{cmax} is the maximum carboxylation rate; Γ^* is the CO_2 compensation point

114   without mitochondrial respiration; K_c and K_o are the Michaelis–Menten constants for

115   CO_2 and O_2, respectively; R_d and J are dark respiration in the light and the electron

116   transport rate, respectively; *TPU* is the rate of triose phosphate export from the

117   chloroplasts. *C* is C_i for the g_m infinite model or CO_2 concentration inside the

118   chloroplasts (C_c) for the g_m finite models, which can be determined using Eqns. 9 and

119   10. *J* is modeled as a function of incident photosynthetically active radiation (*PAR*),

120   which is calculated either using the Smith equation (Eqn. 5) (Harley and Tenhunen,

121   1991; Xu and Badocchi, 2003; Owen *et al.*, 2007; Xue *et al.*, 2017) or the non-

122   rectangle hyperbola equation (Eqn. 6) (Farquhar *et al.*, 1980; Medlyn *et al.*, 2002;

123   Sharkey *et al.*, 2007; Rogers *et al.*, 2017; Kumarathunge *et al.*, 2019) as follows:

124   $$J = \frac{\alpha PAR}{\left(1 + \frac{\alpha^2 PAR^2}{J^2_{max}}\right)^{\frac{1}{2}}} \qquad \text{(Eqn 5)}$$

125   $$\Theta J^2 - (\alpha PAR + J_{max})J + \alpha PAR J_{max} = 0 \qquad \text{(Eqn 6)}$$

126   where α is the quantum yield of electron transport; Θ is the curvature of the non-

127   rectangle hyperbola equation (Table 1); and J_{max} is the maximum electron transport rate.

128   Despite   formulas   for   *J*   calculation   between   the   Smith   and   non-

129   rectangle hyperbola models are different, similar values in *J* were obtained between

130   them. The non-rectangle hyperbola model has been broadly applied in most TBMs

131   (Rogers *et al.*, 2017; Kumarathunge *et al.*, 2019). Hence, the g_m infinite and finite

132   models that consider the non-rectangle hyperbola model were performed in following

133   parts.

134   Under well-watered conditions, the correlation between photosynthetic parameters

135   and temperature can be expressed by the peak Arrhenius function (Dreyer, 2001;

136   Medlyn *et al.*, 2002; Xue *et al.*, 2017; Kumarathunge *et al.*, 2019; Knauer *et al.*, 2019)

137   as follows:

138   $$V_{cmax}/J_{max}/g_m = \frac{k_{25}e^{\Delta H_a(T_k-298.1)/298.1/R/T_k}}{1 + e^{(\Delta S T_k - \Delta H_d)/R/T_k}}\left(1 + e^{(298.1\Delta S - \Delta H_d)/R/298.1}\right) \quad \text{(Eqn 7)}$$

139   where k_{25} is the photosynthetic parameter value at 25°C ($V_{cmax,25}$, $J_{max,25}$, or $g_{m,25}$); ΔH_a

140   is the activation energy; ΔH_d is the deactivation energy; ΔS is the entropy term which

141   characterizes the changes in reaction rate caused by substrate concentration (Table 1);

142   T_k is leaf temperature in Kelvin unit; and *R* is the gas constant (8.314 Pa m³ K⁻¹ mol⁻¹).

143   V_{cmax}, J_{max}, and g_m can be estimated from field measurements, whereas C remains

144   unknown in the leaf photosynthesis model. The leaf photosynthesis model is therefore

145   required to be coupled with the stomatal conductance sub-model for predicting the

146   behavior of stomatal conductance by depending on environmental drivers and A_n. The

147   stomatal conductance sub-model can be expressed as follows:

148    $$g_{sw} = g_{min} + g_{fac} \frac{A_n}{(C_s - \Gamma^*) \times \left(1.0 + \frac{VPD}{a}\right)}$$ (Eqn 8)

149   where a is a constant (default as 35kPa); g_{min} is the value of g_{sw} when A_n is zero; g_{fac} is

150   the stomatal sensitivity to the assimilation rate; and VPD is the vapor pressure deficit

151   between the leaf surface and atmosphere; g_{sw} is the stomatal conductance to water vapor;

152   and g_{fac} and g_{min} are the slope and intercept of the linear relationship between g_{sw} and

153   A_n, respectively, which were extracted from the diurnal gas exchange data.

154   To predict the response of A_n to leaf temperature at ambient and relatively high

155   CO_2 concentrations and light saturation levels (i.e. A_{max}–T_{leaf} curve) for the species

156   derived from literature, we needed to determine the g_{fac} and g_{min} values, without the

157   diurnal gas exchange information. According to our field measurements, g_{fac} was set to

158   3.0 for the woody species and 4.0 for the herbaceous species. The g_{min} was set to 10.0

159   mmol m^{-2} s^{-1} for both C_3 woody and herbaceous species, as commonly adopted by most

160   TBMs (Sellers *et al*., 1996). An initial value was set for C, and then, A_n was determined

161   using Eqn. 1. The known A_n was substituted into Eqn. 8 for g_{sw} estimation, which in

162   turn was substituted into Eqn. 9 or 10 to generate a new C value. The new C value was

163   then compared with the previous value. This new C value was adjusted and then

164   considered as the second initial value for Eqn. 1 until the difference between the

165   generated C and the previous one became less than 0.05 ppm. The iteration procedure

166   used here (i.e. the Newton–Raphson iteration method) was consistent with that used by

167   most TBMs (Dai *et al*., 2003; Sellers *et al*., 1996).

168   **Table 1** Input parameters of the g_m finite photosynthesis-transpiration coupled model. Fixed values
169   were referred to Harley and Tenhunen (1991), Xue *et al*. (2017), Knauer et al. (2019) and
170   Kumarathunge *et al*. (2019). The Rubisco kinetic parameters (K_c, K_o, and Γ^*) were modeled by the
171   Arrhenius function, i.e. [exp(c-$\Delta H_a/R/T_k$)].

Input parameters	Value	Unit	Parameter estimation and expression
$V_{cmax,25}$		µmol m^{-2} s^{-1}	A_n/C_i curves, Eqn. 7

$\Delta H_a (V_{cmax})$		J mol^{-1}	
$\Delta S (V_{cmax})$		J K^{-1} mol^{-1}	
$\Delta H_d (V_{cmax})$	200000	J mol^{-1}	Fixed value
$J_{max,25}$		μmol m^{-2} s^{-1}	A_n/C_i curves, Eqn. 7
$\Delta H_a (J_{max})$		J mol^{-1}	
$\Delta S (J_{max})$		J K^{-1} mol^{-1}	
$\Delta H_d (J_{max})$	200000	J mol^{-1}	Fixed value
$g_{m,25}$		mmol m^{-2} s^{-1}	A_n/C_i curves and chlorophyll
$\Delta H_a (g_m)$		J mol^{-1}	fluorescence, anatomical traits,
$\Delta S (g_m)$		J K^{-1} mol^{-1}	Eqn. 7
$\Delta H_d (g_m)$	200000	J mol^{-1}	Fixed value
g_{fac}		unitless	Diurnal gas exchange, Eqn. 8
g_{min}		mmol m^{-2} s^{-1}	
g_{max}	900	mmol m^{-2} s^{-1}	Fixed value
O_2	210	mmol mol^{-1}	Fixed value
α	0.24	unitless	Fixed value
Θ	0.85	unitless	Fixed value
$R_{d,25}$		μmol m^{-2} s^{-1}	Gas exchange measurement
$\Delta H_a (R_d)$		J mol^{-1}	Xue *et al.* (2017)
$\Delta H_a (K_o)$	23720	J mol^{-1}	
$c (K_o)$	14.68	mmol mol^{-1}	
$\Delta H_a (K_c)$	80990	J mol^{-1}	Bernacchi *et al.* (2002)
$c (K_c)$	38.28	μmol mol^{-1}	
$\Delta H_a (\Gamma^*)$	24460	J mol^{-1}	
$c (\Gamma^*)$	13.49	μmol mol^{-1}	

172

(1) The g_m infinite model and parameterization

In the g_m infinite model, the CO_2 diffusion conductance from intercellular airspace to the chloroplast stroma was assumed to be infinitely large, a common practice in line with almost all TBMs. Photosynthesis is considered to be limited either by stomatal aperture/closure or by CO_2 fixation, which depends on the functioning of leaf photochemistry and/or photosynthetic enzymes. C is the intercellular CO_2 concentration. According to the Fick's first law, C can be expressed as:

$$C = C_s - 1.56 A_n / g_{sw} \qquad \text{(Eqn 9)}$$

where C_s is leaf surface CO_2 concentration.

The apparent maximum carboxylation rate (V_a) was estimated using the linear phase of the A_n/C_i curve (C_i from 50 to 200 ppm) and the apparent maximum electron transport rate (J_a) was estimated using the saturated phase ($C_i > 400$ ppm) by referring to the studies by Xu and Badocchi (2003) and Kumarathunge *et al.* (2019). Input parameters for the g_m infinite model were clarified in Methods S1.

187

(2) The g_m finite model and parameterization

In the g_m finite model, the total conductance of CO_2 diffusion from the leaf surface to the chloroplast stroma consists of g_{sw} and g_m. Photosynthesis is limited by three major factors: stomatal conductance, mesophyll conductance, and biochemical/photochemical limitations. C is the CO_2 concentration inside the chloroplasts that depends on A_n, g_{sw}, g_m, and C_s. It can be expressed according to the Fick's first law as follows:

$$C = C_s - A_n(1.56/g_{sw} + 1.0/g_m) \qquad \text{(Eqn 10)}$$

V_{cmax} and J_{max} are the maximum carboxylation rate and the maximum electron transport rate based on the CO_2 concentration in the chloroplasts, respectively. In this study, V_{cmax}, J_{max}, and g_m values were estimated using four different parameter estimation methods. The Bayesian retrieval algorithm (Zhu *et al*., 2011; Han *et al*., 2020) and the Sharkey online calculator (Sharkey *et al*., 2007) were used to estimate V_{cmax}, J_{max}, and g_m values by using the A_n/C_i curve (abbreviated as V_{cmax_B}, J_{max_B}, g_{m_B} and V_{cmax_S}, J_{max_S}, and g_{m_S}, respectively). The chlorophyll fluorescence–gas exchange method was used to estimates g_m by using the variable J method (abbreviated as g_{m_F}), according to methods used in studies by Harley *et al*. (1992), Niinemets *et al*. (2009), Xue *et al*. (2016; 2017), and Carriquí *et al*. (2020; 2021). The anatomy method for g_m estimation is constrained to a narrow range of leaf temperature around 25ºC ($g_{m\_A,25}$) (Tosens *et al*., 2012; Tomas *et al*., 2013). In this study, the prior range of parameters for the Bayesian retrieval algorithm adopted the range recommended by Zhu *et al*. (2011) and Han *et al*. (2020). The prior ranges of R_d for woody plants and herb plants were 0.01–2.0 µmol m^{-2} s^{-1} and 0.01–5.0 µmol m^{-2} s^{-1}, respectively. Notably, the unit of g_m estimated using the Sharkey online calculator and the Bayesian retrieval algorithm was µmol m^{-2} s^{-1} Pa^{-1}; therefore, it was required to be converted into mol m^{-2} s^{-1} by using the formula: $[(g_m(\text{mol m}^{-2}\,\text{s}^{-1}) = g_m(\text{µmol m}^{-2}\,\text{s}^{-1}\,\text{Pa}^{-1}) \times P/10]$, where P is the actual atmospheric pressure (Pa). Dynamic changes in apparent g_m in response to light environments were not of main concern in the current version of the g_m finite model.

217   V_{cmax}, J_{max}, and g_m estimated using the Sharkey online calculator, Bayesian

218   retrieval algorithm, chlorophyll fluorescence–gas exchange method, and anatomy

219   method were grouped to develop eight parameterization solutions to drive the g_m finite

220   and infinite models (Table 2). The explicit clarity on the parameter values assumed for

221   each parameter estimation method was referred to the Methods S1. For the plant species

222   without $g_{m\_A,25}$ data, model parameterization solutions adopted g_{m_B}, g_{m_S}, and g_{m_F}.

223   g_{m_FA} at a leaf temperature of 25ºC was the mean of $g_{m\_F,25}$ and $g_{m\_A,25}$. g_{m_FA} values at

224   other temperatures were approximated by g_{m_F} only.

225 **Table 2** Eight parameterization solutions considered to drive the g_m infinite and finite
226 photosynthesis–transpiration coupled models. V_a: the apparent maximum carboxylation rate; J_a: the
227 apparent maximum electron transport rate; V_{cmax_B}: V_{cmax} estimated using the Bayesian retrieval
228 algorithm; V_{cmax_S}: V_{cmax} estimated using the Sharkey online calculator; V_{cmax_SB}: the mean of V_{cmax_B}
229 and V_{cmax_S}; J_{max_B}: J_{max} estimated using the Bayesian retrieval algorithm; J_{max_S}: J_{max} estimated
230 using the Sharkey online calculator; J_{max_SB}: the mean of J_{max_B} and J_{max_S}; g_{m_B}: g_m estimated using
231 the Bayesian retrieval algorithm; g_{m_S}: g_m estimated using the Sharkey online calculator; g_{m_F}: g_m
232 estimated using the chlorophyll fluorescence–gas exchange method; $g_{m\_A,25}$: g_m estimated using the
233 anatomy method; g_{m_SBFA}: the mean of g_{m_S}, g_{m_B}, g_{m_F} and $g_{m\_A,25}$; and g_{m_FA}: the mean of g_{m_F} and
234 $g_{m\_A,25}$.

Solution No.	Solution abbreviation	Configuration of each parameterization solution	Model type
1	S_S	$V_{cmax\_S} + J_{max\_S} + g_{m\_S}$	The g_m finite model
2	S_SBFA	$V_{cmax\_S} + J_{max\_S} + g_{m\_SBFA}$	
3	S_FA	$V_{cmax\_S} + J_{max\_S} + g_{m\_FA}$	
4	B_B	$V_{cmax\_B} + J_{max\_B} + g_{m\_B}$	
5	B_SBFA	$V_{cmax\_B} + J_{max\_B} + g_{m\_SBFA}$	
6	B_FA	$V_{cmax\_B} + J_{max\_B} + g_{m\_FA}$	
7	SB_FA	$V_{cmax\_SB} + J_{max\_SB} + g_{m\_FA}$	
8	Inf	$V_a + J_a$	The g_m infinite model

235

236 **Data collection for model validation**

237   V_{cmax}, J_{max}, and g_m estimations by the four parameter estimation methods were

238   performed using field measurements of the A_n/C_i curve plus chlorophyll fluorescence

239   at leaf temperatures ranging from 10-15°C to 40°C in 19 species under 31 experimental

240   treatments (four tropical deciduous tree species, four deciduous broadleaf tree species,

241   seven evergreen broadleaf tree species, three C_3 crops species, and one C_3 herb and

242   grass species) (Methods S2 and S3). Diurnal gas exchange rates were measured in 15

243   species under 25 treatments (Methods S2 and S3). Leaves were sampled *in-situ*

244 immediately after the gas exchange measurement to determine the leaf anatomical

245 structure (Methods S4). For parameter correlation analysis, the A_n/C_i curve and

246 chlorophyll fluorescence data at a leaf temperature of 25°C in seven gymnosperms

247 specie, five ferns species and four herbs species were collected from literature (Carriquí

248 *et al*., 2020; Nadal *et al*., 2018) (Methods S5). For the T_{optA}–T_{opt_gm} correlation analysis,

249 data on T_{optA} and optimum temperature of g_m (T_{opt_gm}) estimated using the carbon

250 isotope discrimination method ($g_{m\_}^{13}C$) and the chlorophyll fluorescence–gas exchange

251 method in five C_3 crops species, two C_3 herbs and grasses species, and one deciduous

252 broadleaf tree species were collected from literature (Evans and von Caemmerer, 2013;

253 Li *et al.,* 2020; Scafaro *et al.*, 2011; von Caemmerer and Evans, 2015; Warren and

254 Dreyer, 2006; Xue *et al*., 2016) (Methods S6). Abbreviations of sampled species under

255 different experimental treatments were referred to Methods S2–S6.

256

257 **Evaluations of the g_m infinite and finite models**

258 Independent field data, including the A_{max}–T_{leaf} curve, T_{optA}, and diurnal gas

259 exchange, were used to validate the g_m infinite and finite models. We fitted the A_{max}–

260 T_{leaf} curve in Eqn. 11 to obtain T_{optA} (Sall and Pettersson, 1994; Battaglia *et al*., 1996;

261 Gunderson *et al*., 2009; Kumarathunge *et al*., 2019),

262 $$A_{max} = A_{opt} - b(T_{leaf} - T_{optA})$$ (Eqn 11)

263 where A_{opt} is the A_n at T_{optA}, and parameter b (unitless) describes the curvature of A_{max}

264 and T_{leaf}.

265 Root mean square error (RMSE) and Nash-Sutcliffe efficiency (NSE) coefficients

266 were used to quantify the performance of the model (Methods S7).

267 Variation in the Rubisco kinetic parameters measured *in vitro* was less than 10%

268 amongst C_3 plant species (von Caemmerer, 2020); thus these parameters can be

269 assumed to be identical for all vegetation types. In this study, the use of the Rubisco

270 kinetic parameters (K_c, K_o, and Γ^*) for the g_m finite model was consistent with

271 Bernacchi *et al*. (2002). However, Knauer *et al*. (2019; 2020) used two types of Rubisco

272 kinetic parameters for model comparisons, of which one type was adopted from the

10

273   study by Bernacchi *et al*. (2002) for the g_m finite model and the other type was adopted

274   from a study by Bernacchi *et al*. (2001) for the g_m infinite model. Similarly, the Rubisco

275   kinetic parameters in study of Bernacchi *et al*. (2001) were used for parameterization

276   of the g_m infinite model in 141 C_3 species by the study of Kumarathunge *et al*. (2019).

277   The hypotheses proposed by Knauer *et al*. (2019; 2020) and Kumarathunge *et al*. (2019)

278   were evaluated by results in our study. Hence, it is necessary here to parameterize the

279   g_m infinite model by using the 2001 version in association with the Rubisco kinetic
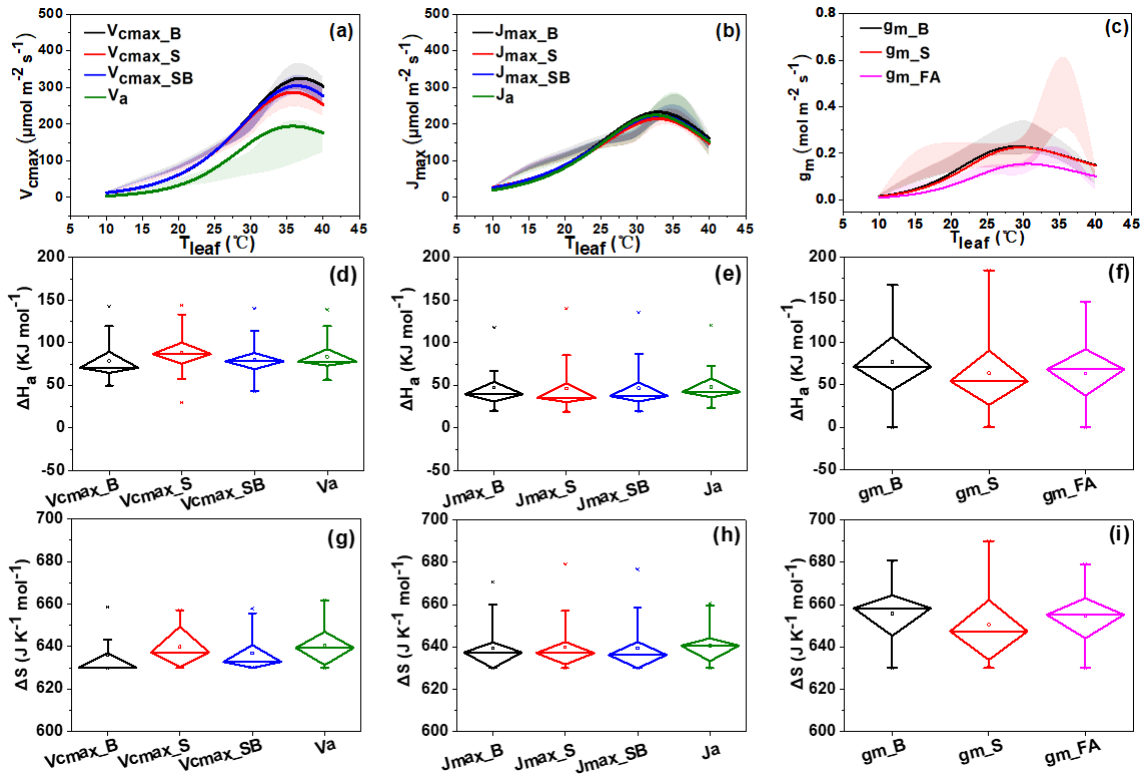
280   parameters.

281

282   **Results**

283   **Temperature responses of V_{cmax}, J_{max}, and g_m**

284   The temperature curve-fitting lines for V_{cmax_B}, V_{cmax_S}, V_{cmax_SB}, and V_a increased

285   rapidly with increase in T_{leaf} from 10°C to 35°C, and began to decrease after reaching a

286   peak (about 300 μmol m^{-2} s^{-1} for V_{cmax_B}, V_{cmax_S}, and V_{cmax_SB}; 180 μmol m^{-2} s^{-1} for

287   V_a) at a leaf temperature around 35°C. V_{cmax_B}, V_{cmax_S}, and V_{cmax_SB} presented a similar

288   behavior ($p > 0.1$, Fig. 1a and Figs. S1a-ae), except at high leaf temperatures ≥ 35°C.

289   Despite V_{cmax_SB} was significantly higher by 43.9% in average than V_a at 25°C,

290   considerable scatter in the difference for the two variables was observed (Table S1).

291   There were similar values at each leaf temperature among temperature response curves

292   of J_{max_B}, J_{max_S}, J_{max_SB}, and J_a (Fig. 1b), with the difference among them being less

293   than 6% at 25°C and the optimal temperatures changing around 32–34°C (Figs. S2a-ae

294   and Table S2). The g_{m_B} temperature curve-fitting line was overlapped with that of g_{m_S}

295   (Fig. 1c), whereas both had significantly higher values by 69% and 58% than that of

296   g_{m_FA} at 25°C, respectively (Table S3). However, the g_{m_S} temperature curve-fitting line

297   did not well overlap with the 95% confidence interval because of irregular observations

298   in g_{m_S} temperature response among sampled species/treatments (Figs. S3a-ae). The

299   temperature curve-fitting lines for g_{m_B}, g_{m_S}, and g_{m_FA} exhibited larger variations in

300   $T_{opt\_g_m}$, ranging from 27 to 32°C, which were lower by 15.7% and 10.6% in average as

301   compared to optimal temperatures for V_{cmax} (i.e. V_{cmax_B}, V_{cmax_S}, and V_{cmax_SB}) and J_{max}

11

302   (i.e. J_{max_B}, J_{max_S}, J_{max_SB}), respectively.

303   The boxplot minimum value of ΔH_a was 49.2 KJ mol^{-1} for V_{cmax_B}, 52.3 KJ mol^{-1}

304   for V_{cmax_S}, 37.6 KJ mol^{-1} for V_{cmax_SB}, and 65.6 KJ mol^{-1} for V_a (Fig. 1d). For J_{max_B},

305   J_{max_S}, J_{max_SB}, and J_a, their minimum values were 22.2, 20.8, 22.6, and 23.6 KJ mol^{-1},

306   respectively (Fig. 1e). Similarities in the minimum value that was close to zero were

307   observed for g_{m_B}, g_{m_S}, and g_{m_FA} (Fig. 1f). Zero value in ΔH_a was found in Pop_WC

308   for g_{m_B}, in Pop_CW for g_{m_S}, and in E_sal and E_mdel for g_{m_FA} (Table S3 and Figs.

309   S3u, t, q, and r). The proportion of species that exhibited a clear temperature response

310   was 95% for g_{m_B}, 95% for g_{m_S}, and 90% for g_{m_FA}. There were similarities in the

311   interquartile range (IQR) of ΔH_a among V_{cmax_B}, V_{cmax_S}, V_{cmax_SB}, and V_a, so did the

312   ΔH_a of the four J_{max} types and the ΔH_a of the three g_m types. However, larger ranges in

313   the IQR of ΔH_a for g_m (i.e. g_{m_B}, g_{m_S}, and g_{m_FA}) than those of J_{max} and V_{cmax} were

314   clearly observed and coefficient of variation (CV) in ΔH_a of g_m (i.e. g_{m_B}, g_{m_S}, and

315   g_{m_FA}) was amplified in average by 135.2% (Table S3). The IQR of ΔS for V_{cmax_B},

316   V_{cmax_S}, V_{cmax_SB}, and V_a was 5.1, 20.2, 8.3, and 15.6 J K^{-1} mol^{-1}, respectively (Fig. 1g).

317   Similarities in the IQR of ΔS among J_{max_B}, J_{max_S}, J_{max_SB}, and J_a temperature responses

318   were evident (Fig. 1h and Table S2). Whereas, the first quartile (Q1) values of ΔS for

319   g_m (i.e. g_{m_B}, g_{m_S}, and g_{m_FA}) were similar or slightly higher than the third quartile (Q3)

320   values of V_{cmax} (i.e. V_{cmax_B}, V_{cmax_S}, and V_{cmax_SB}) and J_{max} (i.e. J_{max_B}, J_{max_S}, and J_{max_SB})

321   (i.e. mean of the Q1 value for g_m was 644.5J K^{-1} mol^{-1}; mean of the Q3 value for V_{cmax}

322   was 644.1 J K^{-1} mol^{-1}, and mean of the Q3 value for J_{max} was 647.5 J K^{-1} mol^{-1}). The

323   mean value of ΔS across g_{m_B}, g_{m_S}, and g_{m_FA} temperature curves was 654 J K^{-1} mol^{-1}

324   ^{1}, whereas it was 639 J K^{-1} mol^{-1} for J_{max} (i.e. J_{max_B}, J_{max_S}, and J_{max_SB}) and 637 J K^{-1}

325   mol^{-1} for V_{cmax} (i.e. V_{cmax_B}, V_{cmax_S}, and V_{cmax_SB}) (Table S1–S3). The CVs of ΔS for

326   g_{m_B}, g_{m_S}, and g_{m_FA} temperature curves were 1.74%, 2.88%, and 2.2%, respectively,

327   while the corresponding CVs of ΔH_a were 58.45%, 78.98%, and 53.26%, respectively

328   (Table S3). These results suggested: greater variations in ΔH_a and ΔS of g_m than those

329   of V_{cmax} and J_{max}; large variations in ΔH_a and relatively small variations in ΔS for g_m;

330   and greater values in ΔS for g_m than those for V_{cmax} and J_{max}.

Fig. 1 V_a and V_{cmax}, J_a and J_{max}, and g_m temperature response curves performed by fitting the mean of parameter estimations of 19 species at 31 treatments using the Eqn. 7 and were labeled by shadow zones (Figs. 1a-c). The shadow zone for each curve-fitting line was the 95% confidence interval of parameter estimations of all sampled species/treatments. Distribution features of ΔH_a and ΔS values that determine V_a and V_{cmax}, J_a and J_{max}, and g_m temperature response curves in all sampled species/treatments were displayed using the box-plot (Figs. 1d-i). The curve-fitting lines of V_a and V_{cmax}, J_a and J_{max}, and g_m temperature response for individual species/treatment were shown in Supporting Information Figs. S1-S3. V_{cmax}, J_{max}, and g_m values were estimated using different parameter estimation methods, namely the Bayesian retrieval algorithm (V_{cmax_B}, J_{max_B}, and g_{m_B}, black solid line), the Sharkey online electronic calculator (V_{cmax_S}, J_{max_S}, and g_{m_S}, red solid line), the mean of V_{cmax_B} and V_{cmax_S} and the mean of J_{max_B}, and J_{max_S} (V_{cmax_SB} and J_{max_SB}, blue solid line), the mean of g_m estimated using the chlorophyll fluorescence–gas exchange and anatomy methods (g_{m_FA}, pink solid line), and the apparent maximum carboxylation rate and the apparent maximum electron transport rate (V_a and J_a, green solid line).

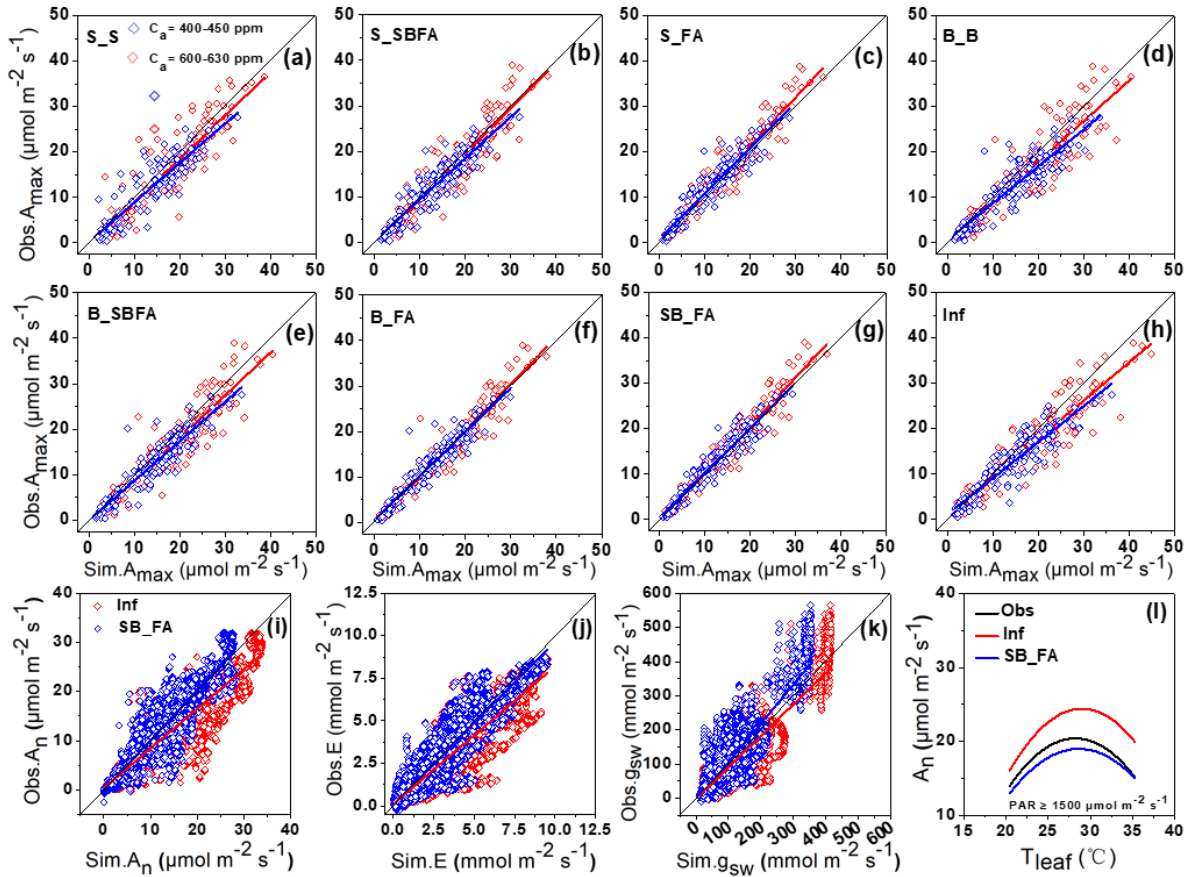**Comparisons between gas exchange observations and simulations by the g_m finite and infinite models**

For the A_{max}–T_{leaf} curves measured at ambient C_a = 400–450 ppm, the slopes of the linear regression between observations and simulations by the S_S, S_SBFA, and S_FA parameterization schemes were 0.87, 0.91, and 1.00, respectively (Figs. 2a-c). The adj.R^2 values for the three schemes were 0.81, 0.86, and 0.90, respectively, and the corresponding NSE values were 0.79, 0.84, and 0.88. The RMSE values of the three parameterization schemes accounted for 24%, 22%, and 19% of the mean A_{max} ($A_{max,mean}$ = 12.47 μmol m^{-2} s^{-1}). The predicted A_{max} values from the S_S and S_SBFA

13

356   schemes were 11% and 7% higher than the $A_{\mathrm{max,mean}}$, respectively (Figs. S4a-ae). These

357   results suggested that g_{m} estimation using the chlorophyll fluorescence–gas exchange

358   method and anatomy method was more reasonable. In line with the results obtained

359   from S_S, S_SBFA, and S_FA schemes, the B_FA scheme fitted A_{max} at each

360   temperature better than the B_B and B_SBFA schemes (Figs. 2d-f and Figs. S4a-ae),

361   which further suggested that the configuration of $g_{\mathrm{m\_FA}}$ for g_{m} estimation was more

362   reasonable. As shown in Figs. 1a and b, the values of $V_{\mathrm{cmax\_B}}$ and $V_{\mathrm{cmax\_S}}$ and those of

363     $J_{\mathrm{max\_B}}$ and $J_{\mathrm{max\_S}}$ at each temperature were similar to each other. Therefore, we

364   considered the possible effects of the combination of V_{cmax} or J_{max} estimations using the

365   Bayesian retrieval algorithm and Sharkey online calculator on A_{max} simulations (the

366   SB_FA scheme in Figs. S4a-ae). The NSE value for the SB_FA scheme was 5% and 1%

367   higher, whereas the ratio of RMSE to $A_{\mathrm{max,mean}}$ was 21% and 12% lower than those for

368   the S_FA and B_FA schemes suggesting better A_{max} predictions using the parameter

369   configuration scheme by considering $V_{\mathrm{cmax\_SB}}$, $J_{\mathrm{max\_SB}}$, and $g_{\mathrm{m\_FA}}$. The adj.R^2, NSE, and

370   the ratio of RMSE to $A_{\mathrm{max,mean}}$ were 0.85, 0.73, and 28%, respectively (Fig. 2h),

371   indicating that although the g_{m} infinite model is generally credible in estimating the

372   A_{max}–T_{leaf} curve, the prediction errors in this model are relatively larger. We found that

373   A_{max} predictions using the g_{m} infinite model were significantly higher (16%) than the

374   observations (partially for 30–40°C, Figs. S4a-ae). Additionally, numerical simulation

375   indicated that the g_{m} finite model driven by the g_{m} temperature function without

376   considering the deactivation stage significantly overestimated A_{max} at higher

377   temperatures 30-35-40°C by 10.99%, 32.51%, 64.06%, respectively. The results

378   obtained from the eight parameterization schemes at C_{a} = 600–630 ppm were similar to

379   those at C_{a} = 400–450 ppm (Figs. 2a-h and Figs. S5a-ae). These results indicated that

380   the g_{m} finite model driven by the SB_FA scheme could predict A_{max} more accurately

381   than the g_{m} infinite model.

382   Figs. 2i-l shows the comparisons in diurnal A_{n}, E, and g_{sw} between observations

383   and predictions using the g_{m} infinite model and the g_{m} finite model that is forced by the

384   parameterization scheme SB_FA (detailed comparisons in each species/treatment

385   shown in Figs. S6-S8). The adj.R^2 values for A_n, E, and g_{sw} predicted using the g_m finite

386   model were 0.88, 0.85, and 0.78, respectively, whereas those predicted using the g_m

387   infinite model were 0.87, 0.83, and 0.76, respectively. The NSE values for the three

388   variables for the g_m finite model were 0.88, 0.85, and 0.76, respectively, and those for

389   the g_m infinite model were 0.76, 0.75, and 0.74, respectively. The ratio of RMSE to the

390   mean of A_n, E, and g_{sw} for the g_m finite model was 27%, 34%, and 40%, respectively,

391   whereas that for the g_m infinite model was 38%, 45%, and 42%, respectively.

392   Meanwhile, significant overestimations in simulated A_n under heat shocking conditions

393   (i.e. T_{leaf} from > 30°C) by 25%–40% by using the g_m infinite model were observed (Fig.

394   2l and Fig. S9). These results suggested that the g_m finite model is superior to the g_m

395   infinite model in predicting diurnal gas exchange under a wide range of growth

396   conditions.

397   For the diurnal changes in A_n, the adj.R^2 and NSE for the g_m finite model were

398   improved by 1% and 12% compared with those for the g_m infinite model. For the diurnal

399   changes in E, the adj.R^2 and NSE for the g_m finite model improved by 2% and 10%

400   compared with those for the g_m infinite model. These results suggested that the effects

401   of g_m finite expression on photosynthesis and transpiration estimations were almost

402   equally stronger.

Fig. 2 Scatter plots showing comparisons in A_{max} observations and predictions between the g_m infinite and finite models that are forced by eight parameterization schemes (Figs. 2a-h, S_S, S_SBFA, S_FA, B_B, B_SBFA, B_FA, SB_FA, and Inf). The blue solid line signifies the linear regression fit between observations at C_a = 400-450 ppm and predictions, and the red solid line signifies the linear regression fit between observations at C_a = 600-630 ppm and predictions. Scatter diagrams in Figs. 2i-k showing comparisons in the diurnal assimilation rate (A_n), transpiration rate (E), and stomatal conductance (g_{sw}) between observations and predictions using the g_m infinite model (red diamonds) and the g_m finite model that is forced by the parameterization scheme SB_FA (blue diamonds). The black solid line represents the 1:1 line. Curve-fitting lines in Fig. 2l show comparisons in diurnal A_n at PAR greater than 1500 µmol m^{-2} s^{-1} and across a wide range of leaf temperatures between observations (black line) and predictions using the g_m infinite model (red line) and the g_m finite model that is forced by the parameterization scheme SB_FA (blue line). C_a: CO_2 concentration at leaf surface; PAR: photosynthetically active radiation.

Statistical correlations between T_{optA} and photosynthetic parameters

The linear regression slope and adj.R^2 values between T_{optA} predictions using the g_m finite model and observations were 0.67 and 0.85, respectively, whereas those obtained using the g_m infinite model were 0.88 and 0.18, respectively (Fig. 3a). T_{optA} predicted using the g_m finite model displayed a better correlation with the observations. We observed that T_{optA} observations had a significant positive correlation with the T_{opt}– g_m values of g_{m_FA} and $g_{m\_}{}^{13}C$ temperature responses, and the adj.R^2 value reached 0.58

16

425   (Fig. 3b). No significant correlations were found among T_{optA}–ΔH_a of g_{m_FA}, T_{optA}–

426   $g_{m\_FA,25}$, and T_{optA}–$J_{max\_SB,25}/V_{cmax\_SB,25}$ (Fig. S10).

427
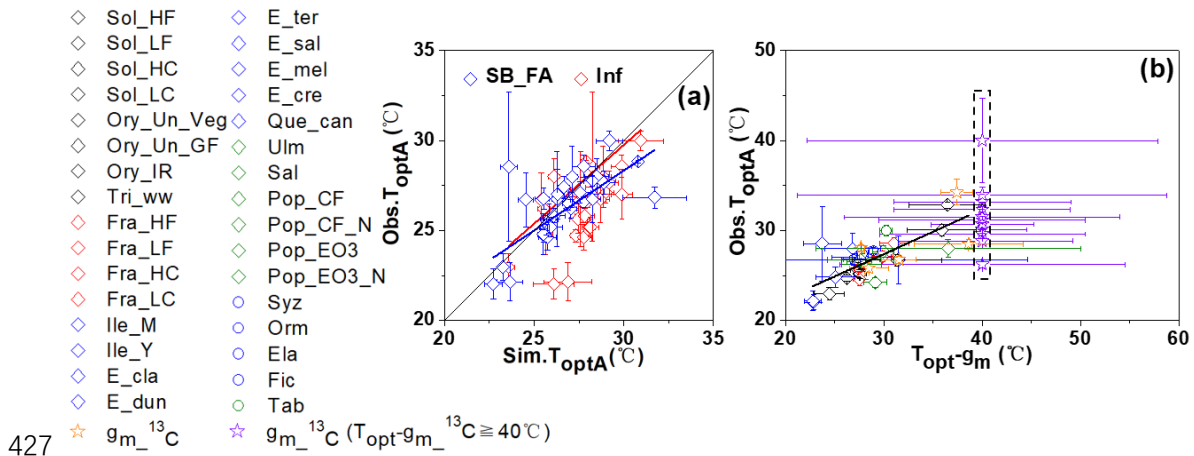
428   **Fig. 3** Scatter diagrams showing comparisons in photosynthesis optimal temperature (T_{optA}) between
429   observations (Obs.T_{optA}) and predictions using the g_m finite model forced by the parameterization
430   solution SB_FA (Sim.T_{optA}, blue circles) and by the g_m infinite model (red circles) (a) and the
431   statistical correlation for Obs.T_{optA} and g_m optimal temperature (T_{opt}-g_m) across different plant
432   functional types (b). The black solid line in Fig. 3a represents the 1:1 line. The red and blue lines in
433   Fig. 3a and the black line in Fig. 3b are the linear regression fit. T_{opt}-g_m in g_m temperature response
434   estimated using the ^{13}C discrimination method greater than and equal to 40°C (T_{opt}-$g_m\_^{13}C$ values ≥
435   40°C were unified to be 40°C shown by purple stars inside the dashed square) was not included for
436   statistical correlation analysis in Fig. 3b. The sampled species/treatments are classified into six plant
437   functional types (PFTs): black diamonds for C_3 crops (C_3C), blue diamonds for evergreen broadleaf
438   trees (EBF), green diamonds for deciduous broadleaf trees (DBF), red diamonds for C_3 herbs and
439   grasses (C_3G), blue circles for tropical evergreen broadleaf trees (TRF), and green circles for tropical
440   deciduous broadleaf trees (TDF).

441

442   **Statistical correlations among photosynthetic parameters**

443   $g_{m\_F,25}$ was positively correlated with $g_{m\_A,25}$, whereas the adjusted R^2 (adj.R^2) was

444   0.22, and the linear regression slope was 0.57, which is much lower than 1.0 (Fig. 4a),

445   primarily because of large discrepancies between the two variables in rice plants. The

446   two variables strongly correlated in other sampled species/treatments with the adj.R^2 of

447   0.76 and the slope of 0.80. A significant exponential correlation was found between

448   $g_{m\_FA,25}$ and $g_{m\_SB,25}$ (adj.R^2 = 0.5, $p < 0.01$, Fig. 4b), with a close agreement found at

449   low $g_m < 0.15$ mol m^{-2} s^{-1}. A negative correlation between $g_{m\_FA,25}$ and the difference

450   for $V_{cmax\_SB,25}$ vs. $V_{a,25}$ was found (adj.R^2 = 0.47, $p < 0.05$, Fig. 4c). $J_{max\_SB,25}$ was closely

451   related to $V_{cmax\_SB,25}$ (adj.R^2 = 0.83, $p < 0.05$, Fig. 4d).
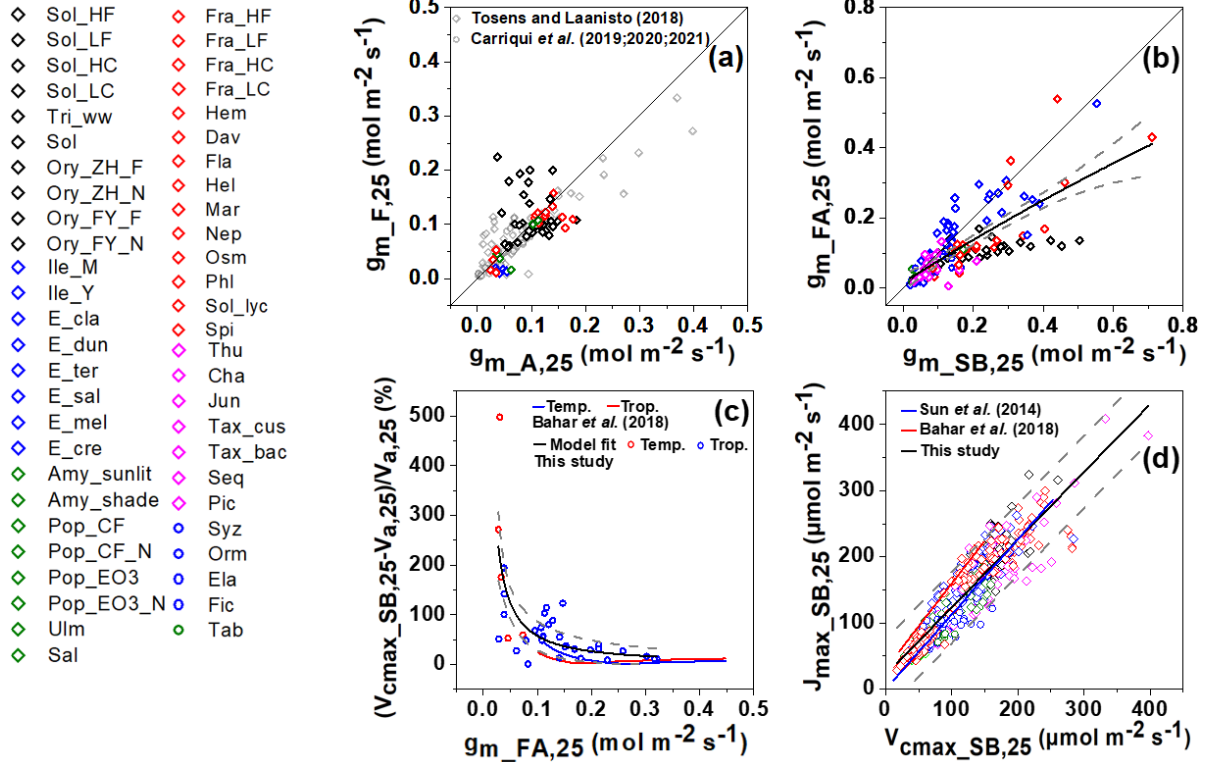
Fig. 4 Statistical correlations for $g_{m\_F,25}-g_{m\_A,25}$ (a), for $g_{m\_FA,25}-g_{m\_SB,25}$ (b), for $g_{m\_FA,25}$–the difference between $V_{cmax\_SB,25}$ and $V_{a,25}$, and for $J_{max\_SB,25}-V_{cmax\_SB,25}$ in sampled species/treatments. The sampled species/treatments in Figs. 4a, b and c are classified into six plant functional types (PFTs): black diamonds for C_3 crops (C_3C), blue diamonds for evergreen broadleaf trees (EBF), green diamonds for deciduous broadleaf trees (DBF), red diamonds for C_3 herbs and grasses (C_3G), blue circles for tropical evergreen broadleaf trees (TRF), and green circles for tropical deciduous broadleaf trees (TDF). $g_{m\_SB,25}$ greater than 1.5 mol m^{-2} s^{-1} are regarded as outliers and are not shown. Gly_amb, Pop_WC, and Pop_CW are not shown as they do not have the observation data at a leaf temperature of 25°C. The paired datasets for $g_{m\_F,25}$ and $g_{m\_A,25}$ in studies of Tosens and Laanisto (2018) and Carriquí *et al.* (2019; 2020; 2021) were added in Fig. 4a (grey diamonds and circles). V_{cmax_Cc} and V_{cmax_Ci} values in temperate species (temp.: *Phyllocladus aspleniifolius*) and tropical species (trop.: *Litsea leefeana*) in the study of Bahar *et al.* (2018) were used to calculate the difference of the two variables as shown in Fig. 4c (blue and red lines, respectively). V_{cmax_Cc} in their study (i.e. $V_{cmax,25}$) was derived from the A_n/C_c curve that is converted from the A_n/C_i curve by assuming a constant g_m at the entire C_i range. V_{cmax_Ci} is the apparent V_{cmax} (i.e. $V_{a,25}$) derived from the A_n/C_i curve in their study, which is equivalent to V_a in our study. The $g_{m,25}$ in their study was estimated using the ^{13}C isotope discrimination method. The dashed lines in grey color represent the 95% prediction intervals of the nonlinear regression.

Discussion

Superiority of the g_m finite model and an optimized parameterization solution

The $A_{max}-T_{leaf}$ curves were accurately predicted using the g_m infinite model only in 15 species/treatments (Figs. S4d, j-s, y, aa, ad, and ae), whereas A_{max} values at higher temperatures (30–40°C) were largely overestimated in other sampled species/treatments. Poor modeling accuracies were also evident in the simulation of

478   diurnal gas exchange rates (Fig. 2l and Figs. S6c, e, h, k, l, n, p, and q). It aligned with

479   the previous reports in rice and winter wheat by Xue *et al*. (2016) and in *Quercus ilex*

480   by Niinemets *et al*. (2009) who found that the photosynthesis model that does not

481   explicitly consider g_m cannot always predict leaf gas exchange accurately. The g_m finite

482   model considers the dependent effects of chloroplast CO_2 concentration on the

483   assimilation rate, stomatal and mesophyll resistance, and leaf surface CO_2

484   concentration (von Caemmerer, 2013; 2020). The relationships among CO_2 diffusion

485   flux, CO_2 concentration gradient between the leaf surface and chloroplasts, and gas

486   diffusion resistance may be approximated using the Fick's first law (Harley *et al*., 1992;

487   Xue *et al*., 2017), as shown in Eqn. 10. Simulation results in gas exchange in 19 species

488   under a wide range of growth conditions proved that the g_m finite model has good

489   transferability and high prediction capacity, due to which the model can be applied to

490   as many C_3 species as possible. The g_m finite model developed in this study can be

491   conveniently substituted into most TBMs by simply replacing ($C_i = C_s$ - $1.56A_n/g_{sw}$) as

492   given in Eqn. 10.

493   V_{cmax}, J_{max}, and g_m temperature responses are key photosynthetic parameters of the

494   g_m finite model. Despite a "one-point" method has been proposed to quantify V_{cmax},

495   there is no consensus that this method can be widely used (Burnett *et al*. 2019). One

496   way to determine V_{cmax} is from the A_n/C_c curve that is converted from the A_n/C_i curve

497   using a value for g_m determined at ambient CO_2 and assuming a constant g_m for the

498   entire range of C_i (Manter and Kerrigan, 2004; Bahar *et al*., 2018). Whereas, the

499   conversion of A_n/C_i to A_n/C_c may not be true at low g_m values under certain conditions

500   (Flexas *et al*., 2007). The key photosynthetic parameters can also be quantified using

501   the curve-fitting method applied to the A_n/C_i curve; for example, the Bayesian retrieval

502   algorithm and the Sharkey online calculator (Sharkey *et al*., 2007; von Caemmerer*et

503   al*., 2009; Gu *et al*., 2010; Zhu *et al*., 2011; von Caemmerer, 2013). Because there exists

504   a curvilinear negative correlation between V_{cmax} estimation and g_m, especially at the

505   lower range of g_m (generally < 0.1 mol m^{-2} s^{-1}) (von Caemmerer, 2013; Bahar *et al*.,

506   2018), the Bayesian retrieval algorithm and/or the Sharkey online calculator may have

507   the equifinality phenomenon for different parameters. For the parameterization of the

508   g_m finite model, V_{cmax}, J_{max}, and g_m values were estimated by the Bayesian retrieval

509   algorithm and the Sharkey online calculator. Additionally, g_m was determined using the

510   chlorophyll fluorescence–gas exchange method and the anatomy method. Our results

511   indicated that the g_{m_B} temperature responses were significantly different from those of

512   g_{m_S} (Figs. S3a-b, d, f-i, l, o-t, y, aa-ac), whereas similarities in the temperature response

513   curve for either V_{cmax} or J_{max} were found between the two curve-fitting methods. It

514   implied that the observed differences in V_{cmax} only at high temperatures between the

515   two methods (Fig. 1a) were likely not related to g_m estimation. A close agreement

516   between the $g_{m\_F,25}$ and $g_{m\_A,25}$ (Fig. 4a) and the T_{opt_gm} between the chlorophyll

517   fluorescence–gas exchange method and the Bayesian retrieval method (adj.R^2 = 0.58

518   and the linear slope = 0.81) was evident, respectively. Furthermore, a close agreement

519   was observed for $g_{m\_FA,25}$ and $g_{m\_SB,25}$, especially at the range of < 0.15 mol m^{-2} s^{-1} (Fig.

520   4b). Results suggested the four parameter estimation methods give similar g_m

521   estimations, especially at the lower range. The estimations in V_{cmax} by the Bayesian

522   retrieval algorithm and the Sharkey online calculator are therefore reasonable,

523   according to the consequence of variations in g_m on estimation of V_{cmax} on C_c and C_i

524   bases (Bahar *et al*., 2018 and Fig. 4c in this study). Finally, we found a significantly

525   linear correlation between $V_{cmax\_SB,25}$ and $J_{max\_SB,25}$ (Fig. 4d), which was similar to the

526   reports by Bahar *et al*. (2018) and Sun *et al*. (2014). Results suggested that the four

527   parameter estimation methods are independent of each other in terms of optimization

528   algorithms and/or principles. In other words, the optimized parameterization scheme

529   (i.e. the SB_FA scheme, discussed below) excludes the equifinality phenomenon.

530   In the present study, a close relationship between $g_{m\_F,25}$ and $g_{m\_A,25}$ was observed

531   in most sampled species/treatments (Fig. 4a). The close correspondence between the

532   two variables has been also reported in many other C$_3$ species (Tosens and Laanisto,

533   2018; Carriquí *et al*., 2019; 2020; 2021) (grey symbols shown in Fig. 4a). Mesophyll

534   conductance is a complex three-dimensional trait that is probably determined by both

535   biochemical and anatomical features. The chlorophyll fluorescence method compares

536   gas exchange signal with the optical signal which may vary with the depth through the

537   mesophyll tissue (Evans, 2021). These variations may explain minor discrepancies

538   between $g_{m\_A,25}$ and $g_{m\_F,25}$ in most sampled species/treatments (Fig. 4a). Carriquí *et al*.

539   (2020) reported that the cell wall composition is a key factor in the g_m setting in

540   sclerophyll species. The constant values in model parameters of the anatomy g_m

541   estimation method for vascular plants such as the ratio of cell wall porosity to tortuosity

542   (P_{cw}) may also contribute to the discrepancies. In this study, $g_{m\_F,25}$ was found to be

543   significantly higher than $g_{m\_A,25}$ in rice. An extremely dense distribution of mesophyll

544   cells in rice was observed (ultrastructure images not shown). The total length of the

545   chloroplast facing the intercellular space (l_c) in association with $g_{m\_A,25}$ by using the

546   ultrathin sections was probably underestimated in rice because of the exclusion of

547   tightly adjacent parts of two mesophyll cells in the sampling fields of view.

548   As shown in Figs. 2a and d, g_m estimation using the A_n/C_i curve only through the

549   Bayesian retrieval algorithm or the Sharkey online calculator can accurately predict leaf

550   gas exchange rates in some species/treatments, whereas cannot in others. A better

551   modeling performance was obtained by the S_FA scheme (i.e. $V_{cmax\_S}+J_{max\_S}+g_{m\_FA}$)

552   than the S_S scheme (i.e. $V_{cmax\_S}+J_{max\_S}+g_{m\_S}$). Our results are similar to reports by

553   Sharkey *et al*. (2007): if chlorophyll fluorescence data are available, it could be possible

554   to estimate g_m from those data to ameliorate reliability of modeling performance. Our

555   results suggested the SB_FA solution (i.e. $V_{cmax\_SB}+J_{max\_SB}+g_{m\_FA)}$ that can predict the

556   photosynthesis and transpiration better than other parameterization solutions as the

557   optimized parameterization solution for the g_m finite model.

558

559   **Temperature responses characteristics of g_m**

560   A g_m response to temperature has been reported in some species, but not in others

561   (Scafaro *et al*., 2011; von Caemmerer and Evans, 2015; Shrestha *et al*., 2019; Evans,

562   2021; Li *et al*., 2020), partially due to differences in g_m estimation methods used by

563   them, as seen in great variations in g_m temperature response obtained by different

564   estimation methods (Fig. 1c and Figs. S3a-ae). We argued that the g_m estimated using

565   the parameter estimation method that can accurately fit the A_{max}–T_{leaf} curve and diurnal

566   gas exchange rates has higher credibility than those that cannot predict accurately.

567   Results of our study suggested that 90% of the sampled species under well-watered

568   conditions exhibit a significant response of g_m to temperature. Inter-species variations

569   in both ΔH_a and ΔS for g_m were significantly greater than those of V_{cmax} and J_{max}. Large

570   variations in ΔH_a signify significant changes in g_m temperature response across species,

571   which is in agreement with the results of the studies by Shrestha *et al*. (2019), von

572   Caemmerer and Evans (2015), and Evans (2021). The two-components modeling

573   method developed by von Caemmerer and Evans (2015) produced ΔH_a for CO_2

574   permeability through the membranes, ranging between 36 and 76 kJ mol^{-1}. Using the

575   isolated pea leaf plasma membranes, Zhao *et al*. (2017) reported ΔH_a for CO_2

576   permeability of 30.2 and 52.4 kJ mol^{-1} at high and low internal carbonic anhydrase (CA)

577   concentrations. Results of our study reported the lower and upper limits of the 95%

578   confidence interval of ΔH_a for g_{m_FA} were 50.14 and 76.12 kJ mol^{-1}, respectively. The

579   determined ΔH_a values of our study are similar to the ranges reported by von

580   Caemmerer and Evans (2015) and Zhao *et al*. (2017). The rates of CO_2 diffusion in the

581   membranes and during the liquid phase reflect the amount of CO_2-permeable and

582   transport enzyme proteins, their thermal stabilities, and the structural components of

583   cell wall. Aquaporins in the membranes and CA inside the vesicles that affect ΔH_a for

584   CO_2 permeability/diffusion (Zhao *et al*., 2017) likely vary greatly in expression levels

585   and the associating heterotetramers among C_3 species (Otto *et al*., 2010; Momayyezi *et*

586   *al.*, 2020). Hence, the determined large variations in temperature response attributes of

587   g_m are reasonable.

588   The temperatures at which V_{cmax} and J_{max} deactivate were usually higher than 35°C

589   and even 40°C in most sampled species. They are similar to the findings in tobacco

590   (Bernacchi *et al*., 2001), rice (Xue *et al*., 2016), and poplar (Silim *et al*., 2010; Xu *et al*.,

591   2020). We found that g_m deactivation temperatures were lower than those for V_{cmax} and

592   J_{max} (Figs. 1a-c), which are similar to reports by Xu *et al*. (2020) and Warren and Dreyer

593   (2006). Meanwhile, better accuracy in leaf gas exchange predictions was obtained using

594   the temperature peak function for g_m than the monotone increasing function. Results

595   highlighted importance of incorporating the deactivation stage of g_m into leaf

596   photosynthesis model for better modeling accuracy. A rapid change in fluidity of plasma

597   membrane was observed within 3 min after heat shock of 37°C in *A. thaliana* (Zheng

598   *et al.*, 2012). Changes in fluidity and permeability of plasma membrane at elevated

599   temperatures (Niu and Xiang, 2018) may cause decline of g_m at supraoptimal

600   temperatures.

601

602   **Effects of the g_m finite expression on photosynthesis and transpiration**

603   Kumarathunge *et al.* (2019) proposed that the variation in T_{optA} among species can

604   be explained by biochemical restrictions ($J_{a,25}/V_{a,25}$). V_a and J_a are referred to as the

605   apparent maximum carboxylation rate and electron transport rate, respectively, and both

606   these parameters, particularly V_a, are numerically and physiologically different from

607   V_{cmax} and J_{max}. A similar result of an asymmetric effect of g_m estimation on V_{cmax} and

608   J_{max} estimations was reported by Manter and Kerrigan (2004) and Sun *et al.* (2014).

609   Hence, we may argue that V_a not only represents the Rubisco carboxylation rate but

610   also embeds the g_m effects. Stripping off the g_m effects from $V_{a,25}$ would cause changes

611   in $J_{a,25}/V_{a,25}$ and then cause significant changes in the T_{optA}–$J_{a,25}/V_{a,25}$ correlation. Our

612   results suggested that T_{optA} has a significant linear correlation with T_{opt_gm} but not JVr,

613   ΔH_a of g_{m_FA}, and $g_{m\_FA,25}$, implying that T_{optA} is probably related to g_m temperature

614   response characteristics.

615   A significant nonlinear correlation between $A_{max,25}$ and $g_{m,25}$ was observed in 271

616   species ($R^2 = 0.73$) (Flexas *et al.*, 2021). g_m limits photosynthesis to an extent similar

617   to that exerted by stomatal and biochemical limitations in vascular plants (Flexas *et al.*,

618   2013). Therefore, a strong correlation between T_{optA} and T_{opt_gm} should be expected.

619   Whereas, the plasticity in T_{optA} was not fully related to g_m because only 58% of the

620   variations in T_{optA} were explained by g_m. Changes in the Rubisco kinetic properties,

621   such as thermal stability of Rubisco activase (Salvucci and Crafts-Brandner, 2004),

622   could be an important mechanism.

23

623   Knauer *et al*. (2020) argued that the g_m finite expression has significant effects on

624   photosynthesis estimation and that the effects of g_m on transpiration are marginal.

625   Conversely, we found that the effects of the g_m finite expression on photosynthesis and

626   transpiration simulations are equally stronger. Significant effects on transpiration

627   estimation were probably achieved through better predictions of g_{sw} because

628   transpiration is a product of *VPD* and g_{sw}. Across diverse species, g_m is strongly linked

629   with g_{sw} and leaf hydraulic conductance through the g_m linkage to extra-xylem

630   components (Flexas *et al*., 2013) such as the plasma membrane intrinsic proteins (PIPs)

631   subfamily of aquaporins (Groszmann *et al*., 2017). Physiological mechanisms

632   underlying the integrated hydraulic–photosynthetic system explained the observed

633   effects of the g_m finite expression on photosynthesis and transpiration.

634

Conclusions

636   In this study, we developed a g_m finite photosynthesis-transpiration coupled model

637   that can be directly applicable for most TBMs and also proposed an optimized

638   parameterization solution. The g_m finite model driven by the parameterization theme of

639   V_{cmax_SB}, J_{max_SB} and g_{m_FA} could well predict A_{max}–T_{leaf} curves and diurnal gas exchange

640   rates in all sampled species under various experimental treatments. However, the g_m

641   infinite model cannot always accurately track variations in photosynthesis and

642   transpiration. Results suggested large variations in ΔH_a and ΔS for g_m. T_{optA} was related

643   to thermal attributes of g_m not *JV*r. Meanwhile, the explicit g_m expression had equally

644   important effects on photosynthesis and transpiration estimations at plant species level.

645   Results of our study proved that the g_m finite expression in most TBMs is important for

646   better understanding effects of g_m on photosynthesis and transpiration under climate

647   change.

648

24

652   (32001129). Sincere thanks are dedicated to prof. John R. Evans at Australian National

653   University for his suggestions on our manuscript draft. We are also grateful to Dandan

654   Liu and Xiao Song for their helps on field data collection and analysis. The authors

655   declare that they have no conflicts of interest.

656

657   **Author contributions**

658   WX: design of the research and funding, data analysis, collection and

659   interpretation, and manuscript writing and revision. HL: data analysis, collection and

660   interpretation, and manuscript writing. JE, MC, MN, TH, and CW: data collection and

661   analysis, manuscript revision. J-F H, J-L Z, Z-G Y and X-W F: data collection and part

662   work of data analysis.

663

664   **Data availability**

665   The data that support the findings of this study are available from the

666   corresponding author upon reasonable request. MATLAB script for Bayesian retrieval

667   algorithm and the g_m finite photosynthesis-transpiration coupled model compiled by

668   FORTRAN can be obtained through directly contacting the correspondence author.

669

670   **References**

671   **Bahar NHA, Hayes L, Scafaro AP, Atkin OK, Evans JR. 2018.** Mesophyll

672   conductance does not contribute to greater photosynthetic rate per unit nitrogen in

673   temperate compared with tropical evergreen wet-forest tree leaves. *New*

674   *Phytologist* **218**: 492–505.

675   **Ball JT, Woodrow IE, Berry JA. 1987.** A model predicting stomatal conductance and

676   its contribution to the control of photosynthesis under different environmental

677   conditions. In: Biggins J, eds. *Progress in Photosynthesis Research*, 221–224.

678   **Barbour MM, McDowell NG, Tcherkez G, Bickford CP, Hanson DT. 2007.** A new

679   measurement technique reveals rapid post-illumination changes in the carbon

680   isotope composition of leaf-respired CO_2. *Plant, Cell & Environment* **30**: 469–482.

681   **Battaglia M, Beadle C, Loughhead S. 1996.** Photosynthetic temperature responses of

682   *Eucalyptus globulus* and *Eucalyptus nitens*. *Tree Physiology* **16**: 81–89.

683 **Bernacchi CJ, Pimentel SE, Portis AR, Long SP. 2001.** Improved temperature
684   response functions for models of Rubisco-limited photosynthesis. *Plant, Cell &*
685   *Environment* **24**: 253–259.

686 **Bernacchi CJ, Portis AR, Nakano H, von Caemmerer S, Long SP. 2002.**
687   Temperature response of mesophyll conductance. Implications for the
688   determination of Rubisco enzyme kinetics and for limitations to photosynthesis in
689   vivo. *Plant Physiology* **130**: 1992–1998.

690 **Burnett AC, Davidson KJ, Serbin SP, Rogers A. 2019.** The "one-point method" for
691   estimating maximum carboxylationcapacity of photosynthesis: A cautionary tale.
692   *Plant, Cell & Environment* **42**: 2472–2481.

693 **Carriquí M, Roig-Oliver M, Brodribb TJ, Coopman R, Gill W, Mark K, Niinemets**
694   **Ü, Perera-Castro1 AV, Ribas-Carbó M, Sack L, Tosens T, Waite M, Flexas J.**
695   **2019.** Anatomical constraints to nonstomatal diffusion conductance and
696   photosynthesis in lycophytes and bryophytes. *New Phytologist* **222**: 1256–1270.

697 **Carriquí M, Nadal M, Clemente-Moreno MJ, Gago J, Miedes E, Flexas J. 2020.**
698   Cell wall composition strongly influences mesophyll conductance in
699   gymnosperms. *The Plant Journal* **103**: 1372–1385.

700 **Carriquí M, Nadal M, Flexas J.** 2021. Acclimation of mesophyll conductance and
701   anatomy to light during leaf aging in *Arabidopsis thaliana*. *Physiologia*
702   *Plantarum* **172**: 1894–1907.

703 **Dai Y, Zeng X, Dickinson RE, Baker I, Bonan GB, Bosilovich MG, Denning AS,**
704   **Dirmeyer PA, Houser PR, Niu G, Oleson KW, Schlosser CA, Yang ZL. 2003.**
705   The common land model. *Bulletin of the American Meteorological Society* **84**:
706   1013-1023.

707 **Dreyer E, Montpied P, Dauder FA, Masson F. 2001.** Temperature response of leaf
708   photosynthetic capacity in seedlings from seven temperate tree species. *Tree*
709   *Physiology* **21**: 223–232.

710 **Evans J, Sharkey TD, Berry JA, Farquhar GD. 1986.** Carbon isotope discrimination

711   measured concurrently with gas exchange to investigate CO_2 diffusion in leaves
712   of higher plants. *Australian Journal of Plant Physiology* **13**: 281–92.

713 **Evans JR, von Caemmerer S. 2013.** Temperature response of carbon isotope
714   discrimination and mesophyll conductance in tobacco. *Plant, Cell & Environment*
715   **36**: 745–756.

716 **Evans JR. 2021.** Mesophyll conductance: walls, membranes and spatial complexity.
717   *New Phytologist* **229**: 1864–1876.

718 **Farquhar GD, von Caemmerer S, Ball JA. 1980.** A biochemical model of
719   photosynthetic CO_2 assimilation in leaves of C_3 species. *Planta* **149**: 78–90.

720 **Flexas J, Diaz-Espejo A, Galmés J, Kaldenhoff R, Medrano H, Ribas-Carbo**
721   **M. 2007.** Rapid variations of mesophyll conductance in response to changes in
722   CO_2 concentration around leaves**.** *Plant, Cell & Environment* **30:** 1284–1298

723 **Flexas J, Barbour MM, Brendel O, Cabrera HM, Carriquí M, Díaz-Espejo**
724   **A, Douthe C, Dreyer E, Ferrio JP, Gago**
725   **J, Gallé A, GalmésJ, Kodama N, Medrano H, Niinemets Ü, Peguero-**
726   **Pina JJ, Pou A, Ribas-Carbó M, Tomás M, Tosens T, Warren CR. 2012.**
727   Mesophyll diffusion conductance to CO_2: an unappreciated central player in
728   photosynthesis. *Plant Science* **193**: 70–84.

729 **Flexas J, Scoffoni C, Gago J, Sack L. 2013.** Leaf mesophyll conductance and leaf
730   hydraulic conductance: an introduction to their measurement and coordination.
731   *Journal of Experimental Botany* **64**: 3965–3981.

732 **Flexas J, Clemente-Moreno MJ, Bota J, Brodribb TJ, Gago J, Mizokami Y, Nadal**
733   **M, Perera-Castro AV, Roig-Oliver M, Sugiura D, Xiong D, Carriquí M. 2021.**
734   Cell wall thickness and composition are involved in photosynthetic limitation.
735   *Journal of Experimental Botany* **72**: 3971-3986.

736 **Gago J, Carriquí M, Nadal M, Clemente-Moreno MJ, Coopman RE, Fernie AR,**
737   **Flexas J. 2019.** Photosynthesis optimized across land plant phylogeny. *Trends in*
738   *Plant Science* **24**: 947-958.

739 **Groszmann M, Osborn HL, Evans JP. 2017.** Carbon dioxide and water transport

740   through plant aquaporins. *Plant, Cell & Environment* **40**: 938–961.

741   **Rogers A, Medlyn BE, Dukes JS, Bonan G, von Caemmerer S, Dietze**
742   **MC, Kattge J, Leakey A, Mercado LM, Niinemets Ü, Prentice IC, Serbin**
743   **SP, Sitch S, Way DA, Zaehle S. 2017.** A roadmap for improving the
744   representation of photosynthesis in Earth system models. *New Phytologist* **213**:
745   22–42.

746   **Gu L, Pallardy SG, Tu K, Law BE, Wullschleger SD. 2010.** Reliable estimation of
747   biochemical parameters from C_3 leaf photosynthesis-intercellular carbon dioxide
748   response curves. *Plant, Cell & Environment* **33**: 1852–1874.

749   **Gunderson CA, O'Hara KH, Campion CM, Walker AV, Edwards NT. 2009.**
750   Thermal plasticity of photosynthesis: the role of acclimation in forest responses to
751   a warming climate. *Global Change Biology* **16**: 2272–2286.

752   **Han T, Zhu G, Ma J, Wang S, Zhang K, Liu X, Ma T, Shang S, Huang C. 2020.**
753   Sensitivity analysis and estimation using a hierarchical Bayesian method for the
754   parameters of the FvCB biochemical photosynthetic model. *Photosynthesis*
755   *Research* **143**: 45–66.

756   **Harley PC, Tenhunen JD. 1991.** Modeling the photosynthetic response of C_3 leaves
757   to environmental factors. *Modeling crop photosynthesis—from biochemistry to*
758   *canopy* **19**: 17–39.

759   **Harley PC, Loreto F, Di Marco G, Sharkey TD. 1992.** Theoretical considerations
760   when estimating the mesophyll conductance to CO_2 flux by analysis of the
761   response of photosynthesis to CO_2. *Plant Physiology* **98**: 1429–1436.

876   **Iqbal WA, Miller IG, Moore RL, Hope IJ, Cowan-Turner D, Kapralov MV. 2021.**
877   Rubisco substitutions predicted to enhance crop performance through carbon
878   uptake modeling. *Journal of Experimental Botany*
879   https://doi.org/10.1093/jxb/erab278.

880   **Knauer J, Zaehle S, De Kauwe MG, Bahar NHA, Evans JR, Medlyn BE,**
881   **Reichstein M, Werner C. 2019.** Effects of mesophyll conductance on vegetation
882   responses to elevated CO_2 concentrations in a land surface model. *Global Change*

883   *Biology* **25**: 1820–1838.

884   **Knauer J, Zaehle S, De Kauwe MG, Haverd V, Reichstein M, Sun Y. 2020.**
885   Mesophyll conductance in land surface models: effects on photosynthesis and
886   transpiration. *The Plant Journal* **101**: 858–873.

887   **Kumarathunge DP, Medlyn BE, Drake JE, Tjoelker MG, Aspinwall MJ, Battaglia**
888   **M, Cano FJ, Carter KR, Cavaleri MA, Cernusak LA, et al. 2019.**Acclimation
889   and adaptation components of the temperature dependence of plant photosynthesis
890   at the global scale. *New phytologist* **222**: 768–784.

891   **Leuning R. 1995.** A critical appraisal of a combined stomatal-photosynthesis model for
892   C_3 plants. *Plant, Cell & Environment* **18**: 339–355.

893   **Li Y, Song X, Li S, Salter WT, Barbour MM. 2020.** The role of leaf water potential
894   in the temperature response of mesophyll conductance. *New phytologist* **225:**
895   1193–1205.

896   **Medlyn B.E, Ellsworth D, Forstreuter M, Harley PC, Kirschbaum MUF, Le Roux**
897   **X, Montpied P, Strassemeyer J, Walcroft A, Wang K, Loustau D. 2002.**
898   Temperature response of parameters of a biochemically based model of
899   photosynthesis. II. A review of experimental data. *Plant, Cell & Environment* **25**:
900   1167–1179.

901   **Manter DK, Kerrigan J. 2004.** A/C_i curve analysis across a range of woody plant
902   species: influence of regression analysis parameters and mesophyll conductance.
903   *Journal of Experimental Botany* **55:** 2581–2588.

904   **Momayyezi M, McKown AD, Bell SCS, Guy RD. 2020.** Emerging roles for carbonic
905   anhydrase in mesophyll conductance and photosynthesis. *The Plant Journal* **101**:
906   831-844.

907   **Niinemets Ü, Díaz-Espejo A, Flexas J, Galmés J, Warren CR. 2009.** Importanceof
908   mesophyll diffusion conductance in estimation of plant photosynthesis inthe field.
909   *Journal of Experimental Botany* **60**: 2271–2282.

910   **Niu Y, Xiang Y. 2018.** An overview of biomembrane functions in plant responses to
911   high-temperature stress. *Frontiers in Plant Science* **9**, 915.

912 **Otto B, Uehlein N, Sdorra S, Fischer M, Ayaz M, Belastegui-Macadam X, …**
913   **Kaldenhoff R. 2010.** Aquaporin tetramer composition modifies the function of
914   tobacco aquaporins. *Journal of Biological Chemistry* **285**: 31253–31260.

915 **Owen KE., Tenhunen J, Reichstein M, Wang Q, Falge E, Geyer R, Xiao X, Stoy P,**
916   **Ammann C, Arain A. 2007.** Linking flux network measurements to continental
917   scale simulations: ecosystem carbon dioxide exchange capacity under non-water-
918   stressed conditions. *Global Change Biology* **13**: 734–760.

919 **Pons TL, Flexas J, von Caemmerer S, Evans JR, Genty B, Ribas-Carbo M,**
920   **Brugnoli E. 2009.** Estimating mesophyll conductance to CO_2: methodology,
921   potential errors, and recommendations. *Journal of Experimental Botany* **60**: 2217–
922   2234.

923 **Sall T, Pettersson P. 1994.** A model of photosynthetic acclimation as a special case of
924   reaction norms. *Journal of Theoretical Biology* **166**: 1–8.

925 **Salvucci ME, Crafts-Brandner SJ. 2004.** Relationship between the heat tolerance of
926   photosynthesis and the thermal stability of Rubisco activase in plants from
927   contrasting thermal environments. *Plant Physiology* **134**: 1460–1470.

928 **Sellers PJ, Randall DA, Collatz GJ, Berry JA, Field CB, Dazlich DA, Zhang C,**
929   **Collelo GD, Bounoua L. 1996.** A revised land surface parameterization (SiB2)
930   for atmospheric GCMS. Part I: model formulation. *Journal of Climate* **9**: 676–705.

931 **Scafaro AP, von Caemmerer S, Evans JR, Atwell BJ. 2011.** Temperature response of
932   mesophyll conductance in cultivated and wild Oryza species with contrasting
933   mesophyll cell wall thickness. *Plant, Cell & Environment* **34**: 1999–2008.

934 **Sharkey TD, Bernacchi CJ, Farquhar GD, Singsaas EL. 2007.** Fitting
935   photosynthetic carbon dioxide response curves for C_3 leaves. *Plant, Cell &*
936   *Environment* **30**: 1035–1040.

937 **Silim SN, Ryan N, Kubien D. 2010.** Temperature response of photosynthesis and
938   respiration in *Populus balsamifera* L.: acclimation versus adaption.
939   *Photosynthesis Research* **104**: 19–30.

940 **Shrestha A, Song X, Barbour MM. 2019.** The temperature response of mesophyll

941   conductance, and its component conductances, varies between species and
942   genotypes. *Photosynthesis Research* **141**: 65–82.

943 **Sun Y, Gu L, Dickinson RE, Pallardy SG, Baker J, Cao Y, DaMatta FM, Dong X,**
944   **Ellsworth D, Van Goethem D, Jensen AM, Law BE, Loos R, Martins SC,**
945   **Norby RJ, Warren J, Weston D, Winter K. 2014.** Asymmetrical effects of
946   mesophyll conductance on fundamental photosynthetic parameters and their
947   relationships estimated from leaf gas exchange measurements. *Plant, Cell &*
948   *Environment* **37**: 978–994.

949 **Tomas M, Flexas J, Copolovici L, Galmes J, Hallik L, Medrano H, Ribas-Carbo**
950   **M, Tosens T, Vislap V, Niinemets Ü. 2013.** Importance of leaf anatomy in
951   determining mesophyll diffusion conductance to CO_2 across species: quantitative
952   limitations and scaling up by models. *Journal of Experimental Botany* **64**: 2269–
953   2281.

954 **Tosens T, Niinemets Ü, Vislap V, Eichelmann H, Castro Diez P. 2012.**
955   Developmental changes in mesophyll diffusion conductance and photosynthetic
956   capacity under different light and water availabilities in *Populus tremula*: how
957   structure constrains function. *Plant, Cell & Environment* **35**: 839–856.

958 **Tosens T, LaanistoL. 2018.** Mesophyll conductance and accurate photosynthetic
959   carbon gain calculations. *Journal of Experimental Botany* **69**: 5315–5318.

960 **von Caemmerer S, Farquhar G, Berry J. 2009.** Biochemical model of C_3
961   photosynthesis. In: Laisk, A., Nedbal, L., Govindjee, eds. *Photosynthesis in silico:*
962   *Understanding complexity from molecules to ecosystems.* Springer Netherlands,
963   Dordrecht, pp. 209–230.

964 **von Caemmerer S. 2013.** Steady-state models of photosynthesis. *Plant, Cell &*
965   *Environment* **36**: 1617–1630.

966 **von Caemmerer S, Evans JR. 2015.** Temperature responses of mesophyll conductance
967   differ greatly between species. *Plant, Cell & Environment* **38**: 629–637.

968 **von Caemmerer, S., 2020.** Rubisco carboxylase/oxygenase: From the enzyme to the
969   globe: A gas exchange perspective. *Journal of Plant Physiology* **252**: 153240.

970 **Warren CR, Dreyer E. 2006.** Temperature response of photosynthesis and internal
971   conductance to CO_2: results from two independent approaches. *Journal of*
972   *Experimental Botany* **57**: 3057–3067.

973 **Xu L, Badocchi D. 2003.** Seasonal trends in photosynthetic parameters and stomatal
974   conductance of blue oak (*Quercus douglasii*) under prolonged summer. *Tree*
975   *Physiology* **23**: 865–877.

976 **Xu Y, Shang B, Feng Z, Tarvainen L. 2020.** Effect of elevated ozone, nitrogen
977   availability and mesophyll conductance on the temperature responses of leaf
978   photosynthetic parameters in poplar. *Tree Physiology* **40**: 484–497.

979 **Xue W, Otieno D, Ko J, Werner C, Tenhunen J. 2016.** Conditional variations in
980   temperature response of photosynthesis, mesophyll and stomatal control of water
981   use in rice and winter wheat. *Field Crops Research* **199**: 77–88.

982 **Xue W, Ko J, Werner C, Tenhunen J. 2017.** A spatially hierarchical integration of
983   close-range remote sensing, leaf structure and physiology assists in diagnosing
984   spatiotemporal dimensions of field-scale ecosystem photosynthetic productivity.
985   *Agricultural and Forest Meteorology* **247**: 503–519.

986 **Zhao M., Tan H-T, Scharwies J, Levin K, Evans JR, Tyerman SD. 2017.** Association
987   between water and carbon dioxide transport in leaf plasma membranes: assessing
988   the role of aquaporins. *Plant, Cell & Environment* **40**: 789–801.

989 **Zheng SZ, Liu YL, Li B, Shang ZL, Zhou RG, Sun DY. 2012.** Phosphoinositide-
990   specific phospholipase C9 is involved in the thermotolerance
991   of Arabidopsis. *The Plant Journal* **69**: 689–700.

992 **Zhu GF, Li X, Su YH, Lu L, Huang CL. 2011.** Seasonal fluctuations and temperature
993   dependence in photosynthetic parameters and stomatal conductance at the leaf
994   scale of *Populus euphratica* Oliv. *Tree physiology* **31**:178–195.

995

996 **Supporting Information**

997 Additional supporting information may be found in the online version of this article:

998 **Fig. S1** The temperature response curves of V_{cmax}.

999 **Fig. S2** The temperature response curves of J_{max}.

Fig. S3 The temperature response curves of g_m.

Fig. S4 Temperature response curves of the net assimilation rate under ambient CO_2 concentration (400–450 ppm) and high radiation derived from field measurements and predictions.

Fig. S5 Temperature response curves of the net assimilation rate under ambient CO_2 concentration (600–630 ppm) and high radiation derived from field measurements and predictions.

Fig. S6 Comparisons in diurnal photosynthesis rate between field observations and predictions.

Fig. S7 Comparisons in diurnal transpiration rate between field observations and predictions.

Fig. S8 Comparisons in diurnal stomatal conductance between field observations and predictions.

Fig. S9 Comparisons in diurnal A_n at PAR greater than 1500 μmol m^{-2} s^{-1} and across a wide range of leaf temperatures between observations and predictions using the g_m infinite model and the g_m finite model that is forced by the parameterization scheme SB_FA.

Fig. S10 Statistical relationships for photosynthesis optimal temperature and the ratio of the maximum carboxylation rate to the maximum electron transport rate (JVr) (a), T_{optA}–$g_{m\_F,25}$ (b), and T_{optA}–activation term of g_{m_F} (ΔH_a) (c).

Table S1 Temperature response characteristic parameters of V_{cmax}.

Table S2 Temperature response characteristic parameters of J_{max}.

Table S3 Temperature response characteristic parameters of g_m.

Methods S1 The explicit clarity on the parameter values assumed for each parameter estimation method

Methods S2

Methods S3

Methods S4

Methods S5

Methods S6

Methods S7